CHAPTER 4

Abundance of PAHs in the Small Magellanic Cloud

The difference in the extinction curve of the Small Magellanic Cloud (SMC) with respect to that of the the Milky Way (MW) and the Large Magellanic Cloud (LMC) has been a subject of interest and the source for various silicate–graphite–Polycyclic Aromatic Hydrocarbon (PAH) based dust models over the years. In this chapter, we have studied the diffuse dust emission in the SMC using observations made in the far-ultraviolet (FUV: 1000–1750 Å) and subsequently compared this diffuse emission with observations made in the infrared for the same locations, in an attempt to constrain the dust component responsible for the observed emissions. Since the weakness or absence of the 2175 Å feature in the SMC extinction curve is associated with the absence of PAH molecules, we have tried to explain the selective absence of this feature in the SMC using our observed correlation trends.

4.1 Introduction and Motivation

The difference in properties of interstellar dust as well as the gas-to-dust ratio from one galaxy to another is well established by the variations seen in the far-ultraviolet (FUV) extinction curves of the Milky Way (MW), the Large Magellanic Cloud (LMC) and the Small Magellanic Cloud (SMC) [134, 135]. In fact, the metallicity of the SMC, Z≈0.005 [136], is smaller by a factor of about 10 in comparison to the MW, as opposed to about 4 for the LMC [137]. Bouchet et al. (1985) [135] found the dust-to-gas ratio in the SMC to be 8 times smaller than the MW while Koornneef (1982) [138] found the same ratio for the LMC to be 4 times smaller than the MW. These properties of the SMC being similar to low-metallicity high-redshift galaxies, and owing to the fact that it is so nearby to the MW (≈60 kpc) [139], make the SMC an ideal system for studying the interstellar medium (ISM) of such galaxies which are in the early stages of their chemical enrichment [140], at high spatial resolution and sensitivity. This is further strengthened by its nearly face-on orientation and low Galactic extinction to the observer in the MW.

Although the SMC provides a dust sample having significantly different characteristics than the MW and LMC dust, the most striking difference between the three is the 2175 Å feature in their extinction curves. Most models assume the SMC dust to typically consist of silicates and attribute the absence of the 2175 Å bump along 4/5 sightlines [21, 134] to a lack of graphite or carbonaceous dust. However, the presence of the bump was observed for a particular location (AzV 456/ SK 143) in the SMC by Gordon et al. (2003) [21] and recently, it has also been observed by Apellaniz & Rubio (2012) [141]. Hence, the 2175 Å bump is not completely absent in the SMC and it's presence or absence seems to be dependent on location/sightline under observation.

The contribution of Polycyclic Aromatic Hydrocarbons (PAHs) towards the 2175 Å bump and FUV rise in the interstellar extinction curve was suggested by Leger et al. (1989) [142], which was supported with experimental data shortly after [143], although observational proof needed to wait until much later [144]. It has already been shown that the extinction curves for these three galaxies can be reproduced by models consisting of amorphous silicates, graphites and PAHs, with appropriate changes in their size distributions and relative abundances for differing sightlines [25, 26]. More recently, Steglich et al. (2010, 2011) [145, 146] have investigated PAH species as potential carriers of the 2175 Å bump using laboratory based techniques. However, it has been observed that for low-metallicity galaxies, the PAH emission is highly deficient [147–150] and this has also been confirmed spectroscopically [151, 152].

As discussed in Chapter 2, stellar continuum-subtracted 8 μm gives PAH emission [153], while Very Small Grain (VSG) or hot dust emission is seen near 24 μm [23, 104, 105] depending on the observed environment [115, 154, 155]. The strength of the local star formation also seems to dictate large variations in the 24 μm emission relative to the 8 μm emission [154]. In addition, the emissions at 65 μm and 90 μm are observed to be from large dust grains or particulate matter and the efficiency of destruction of dust grains due to heating by stellar photons is seen more clearly at shorter wavelengths.

The dissimilarities in the environment caused by enhanced star formation in some regions of the SMC has been suggested to be the reason for the observed difference in the interstellar extinction curves [156]. Hence, we hope to explain the dust properties for our sample of locations which is spread over different environments ranging from those near active star forming or HII regions to those at the outskirts of the SMC, using FUV–IR correlation studies.

4.2 Sample of Observations

Pradhan et al. (2011) [157] had reported the first observations of FUV (1000–1150 Å) diffuse radiation from the SMC using *Far Ultraviolet Spectroscopic Explorer (FUSE)* [158, 159]. They found the FUV diffuse fraction from the SMC to be higher than that of the LMC which was attributed to the higher dust albedo (∼50%) in SMC [25]. Out of 220 observations made using *FUSE* in a 5° radius of the SMC, 190 were of stars and 30 observations were used by them to extract the diffuse background. The diffuse data were obtained using the low-resolution LWRS ($30'' \times 30''$) which was the largest among the three *FUSE* apertures enabling it to collect decent diffuse flux. After background subtraction and avoiding airglow lines, the data were collapsed into two wavelength bands per detector resulting in six bands but they [157] found the data to be of much higher quality from segment 1, leaving four bands with effective FUV wavelengths: 1004 Å (1A1), 1058 Å (1A2), 1117 Å (1B1) and 1157 Å (1B2). In case of multiple observations for the same location, the difference in FUV brightness comes from a slight difference in position, which suggests that the FUSE data may possibly have a large uncertainty or intrinsic scatter. Hence, out of 30, we effectively got 24 different locations for this work.

In order to increase the wavelength coverage of the FUV sample, we have used archival data which was observed by the *International Ultraviolet Explorer (IUE)* telescope [160–162] in the SMC corresponding to the locations observed by *FUSE*. We found 21 locations with *IUE* observations available in the MAST archive at Space Telescope Science Institute (STScI). These observations were made by the Short Wavelength Prime (SWP) camera [160, 161, 163] aboard *IUE* with an aperture size of $20'' \times 10''$ in the 1150-1978 Å wavelength range.

We considered the FUV observations made by Pradhan et al. (2011) [157] and tried to look for archival data in the infrared at the same locations. We found data for all 24 locations in the *Spitzer* and *AKARI* telescope archives at 8 μm, 65 μm and 90 μm. The instrument details for both these space-based IR telescopes have been discussed in Section 1.2.1. However, only 7 out of the 24 observed FUV locations had data available at 24 μm in the *Spitzer* archive. The *Wide-field Infrared Survey Explorer (WISE)* [164] telescope mapped the sky in four wavelength bands: 3.4 μm, 4.6 μm, 12 μm and 22 μm (W1, W2, W3, W4). Hence, we have used data taken by *WISE* in the 22 μm (W4) band with an angular resolution of $12''$ to augment the 24 μm *Spitzer* data. Figure 4.1 shows our 24 locations on a far-IR 65 μm image of the SMC taken by the *AKARI*-FIS (N60 band).

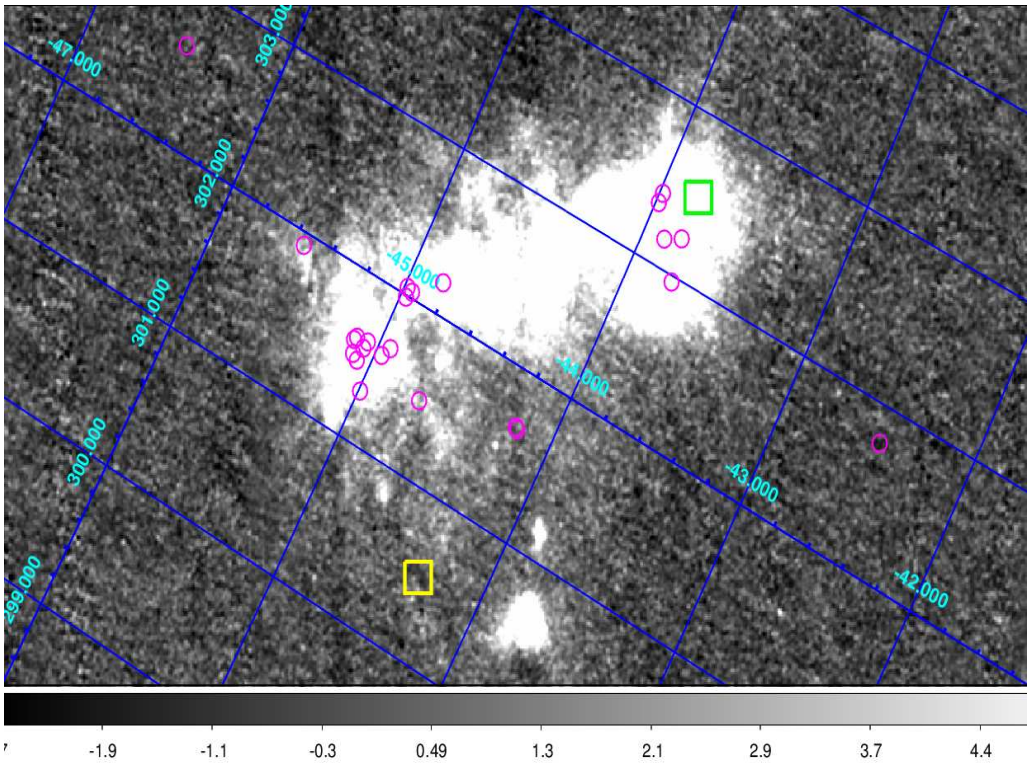

Figure 4.1: The 24 dust locations studied by us are shown as magenta coloured circles on an *AKARI* (65 μm) image. The yellow square represents the location discussed in Gordon et al. (2003) [21] and the green square represents the locations discussed in Apellaniz & Rubio (2012) [141] to have shown the presence of the 2175 Å bump.

4.3 Data analysis and Results

The FUV intensities for the 24 *FUSE* observations at 1004 Å, 1058 Å, 1117 Å and 1157 Å have been taken from Pradhan et al. (2011) [157]. We have used the flux tables available in the *IUE* (MAST) archive to obtain the intensities for 21 locations at three wavelengths: 1250 Å, 1500 Å and 1750 Å, so that we may be able to study the FUV: 1000-1750 Å range at considerable intervals of 250 Å. The *IUE* observations corresponding to the *FUSE* locations are presented in Table 4.1. The three locations with unavailable archival data have been left blank. The *IUE* flux values are shown as I_{1250}, I_{1500} and I_{1750} with the subscript denoting the corresponding wavelength. The locations are given in galactic coordinates (gl, gb) and the uncertainties in the data presented here are the 1σ error values while calculating the fluxes.

We have first convolved all the infrared images taken by *Spitzer*, *WISE* and *AKARI* at 8 μm, 24 μm, 22 μm, 65 μm and 90 μm using a Gaussian kernel to match the *FUSE* LWRS aperture size of $30'' \times 30''$. We have then calculated the median value of intensity within an aperture of size $30'' \times 30''$ for all the convoluted mid-IR (MIR) and far-IR (FIR) data. Next, we repeated the convolution and aperture photometry process for the IR images to match the *IUE* aperture size of $20'' \times 10''$. The calculated IR intensities for *FUSE* convolved data are shown in Table 4.2 while those for *IUE* convolved data are shown in Table 4.3. In both tables, $I_{8\mu m}$, $I_{24\mu m}$, $I_{22\mu m}$, $I_{65\mu m}$ and $I_{90\mu m}$ represent the intensities with the subscript denoting the corresponding wavelength. The locations for which 24 μm data were not found have been kept blank.

Once we had calculated the IR intensities, we then computed the Spearman's rank correlation coefficients (ρ), as described in Section 1.3.2, among the FUV and IR intensities. The results of our correlation studies are presented in Tables 4.4 and 4.5. Table 4.4 shows the rank correlations among the IR (*Spitzer*: 8 μm, 24 μm; *WISE*: 22 μm; *AKARI*: 65 μm, 90μm) and the FUV (*FUSE*: 1004 Å, 1058 Å, 1117 Å, 1157 Å; *IUE*: 1250 Å, 1500 Å, 1750 Å) intensities. While calculating the correlation coefficients, we have compared the UV data with only those IR data which have been convolved for the same aperture size so that all the data is on equal footing, i.e. the *FUSE* UV data has been correlated with IR data presented in Table 4.2 while the *IUE* UV data has been correlated with IR data presented in Table 4.3. The rank correlations among the MIR and FIR data are shown in Table 4.5. As mentioned earlier, the number of locations with 24 μm data was very less which limits our reliability in the observed correlation results for 24 μm vs. FUV. This is why we have used the 22 μm data to augment the 24 μm observations.

Table 4.1: Flux details for 21 FUV diffuse locations available in the *IUE* data archive corresponding to the observations made using the *FUSE* LWRS.

FUSE ID[a]	*IUE* ID	gl[b]	gb[b]	I^c_{1250}	I^c_{1500}	I^c_{1750}
G9310201	SWP33576	303.4160	-43.9837	6.09 ± 0.39	6.66 ± 0.37	5.95 ± 0.19
G9310301	SWP32657	303.3522	-43.9848	1.19 ± 0.09	1.25 ± 0.09	1.33 ± 0.05
G9310401	SWP32634	303.2306	-43.8065	6.12 ± 0.30	6.85 ± 0.32	6.42 ± 0.17
G9310501	SWP07026	303.1724	-43.8871	2.47 ± 0.17	1.97 ± 0.17	1.57 ± 0.07
G9310601	SWP32389	302.9638	-43.7682	0.10 ± 0.03	0.12 ± 0.03	0.09 ± 0.02
F3230101	SWP29730	302.7813	-42.4777	0.03 ± 0.03	0.11 ± 0.04	0.27 ± 0.00
D9110901		302.6293	-46.4968			
G9310701	SWP44978	302.1944	-44.8284	1.52 ± 0.10	2.09 ± 0.23	1.59 ± 0.05
P2030201	SWP37769	302.0468	-44.9842	49.5 ± 1.56	33.4 ± 0.91	22.85 ± 0.41
C1580101	SWP01597	302.0361	-44.9538	14.2 ± 0.87	11.15 ± 0.80	9.1 ± 0.34
S4057101	SWP44978	301.9879	-44.9723	2.31 ± 0.13	2.23 ± 0.11	1.66 ± 0.05
G9310801	SWP43336	301.9201	-45.5506	0.10 ± 0.02	0.14 ± 0.02	0.19 ± 0.01
G9310901	SWP51882	301.6525	-44.9388	1.51 ± 0.10	1.08 ± 0.06	0.78 ± 0.03
G9311002	SWP33300	301.6106	-45.0572	8.21 ± 0.46	6.14 ± 0.30	4.475 ± 0.13
C0830201	SWP45153	301.5995	-45.1168	4.27 ± 0.46	4.36 ± 0.18	2.82 ± 0.08
G0350101	SWP24869	301.5767	-45.1257	1.98 ± 0.13	1.59 ± 0.13	1.28 ± 0.05
E5110802	SWP51639	301.6581	-44.1975	2.64 ± 0.16	2.45 ± 0.14	2.35 ± 0.05
F3210103	SWP04925	301.5848	-44.9657	26.35 ± 2.58	20.30 ± 1.12	11.80 ± 0.34
E5110801		301.6505	-44.1871			
A0750204	SWP23925	301.5607	-45.0648	0.16 ± 0.02	0.09 ± 0.02	0.06 ± 0.01
C0830302		301.4967	-45.1017			
G0350301	SWP27926	301.4725	-45.0704	0.09 ± 0.03	0.04 ± 0.03	0.06 ± 0.02
D9044301	SWP24868	301.4683	-44.6991	2.83 ± 0.15	2.31 ± 0.19	1.49 ± 0.05
D9044401	SWP24871	301.3154	-44.9915	5.17 ± 0.35	4.06 ± 0.24	3.02 ± 0.13

Notes:
[a]The *FUSE* diffuse observation details are presented in Pradhan et al. (2011) [157].
[b]gl and gb are the Galactic longitude and latitude in degrees (°).
[c]The *IUE* FUV data are in units of 10^{-13} ergs cm^{-2} sec^{-1} Å^{-1}.

Table 4.2: Calculated MIR and FIR intensities from the *Spitzer*, *WISE* and *AKARI* archival data for our target 24 SMC locations after convolution for comparison with *FUSE* data.

Sl. No.	gl[a]	gb[a]	$I^b_{8\mu m}$	$I^b_{24\mu m}$	$I^b_{22\mu m}$	$I^b_{65\mu m}$	$I^b_{90\mu m}$
1	303.4160	-43.9837	0.63 ± 0.04	23.73 ± 0.16	17.72 ± 2.20	49.21 ± 1.49	65.41 ± 1.34
2	303.3522	-43.9848	0.31 ± 0.16	19.48 ± 0.22	17.36 ± 2.52	57.78 ± 1.16	68.45 ± 0.91
3	303.2306	-43.8065	0.37 ± 0.09		16.14 ± 2.72	38.53 ± 1.56	47.85 ± 1.57
4	303.1724	-43.8871	0.55 ± 0.16		15.86 ± 2.67	29.56 ± 0.44	42.58 ± 0.62
5	302.9638	-43.7682	0.87 ± 0.02		16.42 ± 2.36	9.61 ± 0.11	16.16 ± 0.31
6	302.7813	-42.4777	2.86 ± 0.82	20.72 ± 5.46	16.27 ± 2.35	1.32 ± 0.00	2.10 ± 0.00
7	302.6293	-46.4968	3.62 ± 1.49	22.38 ± 29.90	21.35 ± 2.26	0.05 ± 0.00	2.05 ± 0.03
8	302.1944	-44.8284	1.07 ± 0.02		16.39 ± 2.36	10.70 ± 0.26	19.84 ± 0.40
9	302.0468	-44.9842	0.50 ± 0.03		15.82 ± 2.42	46.85 ± 2.05	55.31 ± 2.06
10	302.0361	-44.9538	0.49 ± 0.03	22.81 ± 0.17	17.36 ± 2.52	47.33 ± 2.27	52.00 ± 2.24
11	301.9879	-44.9723	0.30 ± 0.03		15.95 ± 2.69	27.52 ± 1.11	32.57 ± 1.26
12	301.9201	-45.5506	0.60 ± 0.01	17.85 ± 0.03	14.94 ± 2.57	2.94 ± 0.05	8.23 ± 0.21
13	301.6525	-44.9388	0.42 ± 0.05		15.86 ± 2.66	10.53 ± 0.15	19.90 ± 0.16
14	301.6106	-45.0572	0.68 ± 0.07		15.62 ± 2.69	42.02 ± 0.66	58.05 ± 0.48
15	301.5995	-45.1168	0.59 ± 0.12		15.66 ± 2.64	16.52 ± 0.32	30.37 ± 0.52
16	301.5767	-45.1257	0.67 ± 0.09		16.55 ± 2.39	14.34 ± 0.31	25.14 ± 0.53
17	301.6581	-44.1975	1.19 ± 0.00		15.47 ± 2.60	1.14 ± 0.09	5.38 ± 0.03
18	301.5848	-44.9657	0.09 ± 0.00		14.73 ± 2.53	15.85 ± 0.24	22.93 ± 0.09
19	301.6505	-44.1871	1.19 ± 0.00		14.50 ± 2.50	1.02 ± 0.08	5.53 ± 0.03
20	301.5607	-45.0648	0.91 ± 0.03		16.39 ± 2.75	26.24 ± 1.24	37.09 ± 1.67
21	301.4967	-45.1017	1.01 ± 0.01		15.69 ± 2.65	19.01 ± 1.36	25.51 ± 1.04
22	301.4725	-45.0704	1.03 ± 0.04		16.63 ± 2.40	24.32 ± 2.17	32.18 ± 1.90
23	301.4683	-44.6991	1.03 ± 0.01	17.66 ± 0.04	16.39 ± 2.36	3.29 ± 0.05	7.91 ± 0.10
24	301.3154	-44.9915	0.70 ± 0.03		14.59 ± 2.51	10.31 ± 0.31	17.26 ± 0.38

Notes:
[a]gl and gb are the Galactic longitude and latitude in degrees (°).
[b]The MIR and FIR data are in units of MJy sr^{-1}.

Table 4.3: Calculated MIR and FIR intensities from the *Spitzer*, *WISE* and *AKARI* archival data for our target 24 SMC locations after convolution for comparison with *IUE* data.

Sl. No.	gl[a]	gb[a]	$I^b_{8\mu m}$	$I^b_{24\mu m}$	$I^b_{22\mu m}$	$I^b_{65\mu m}$	$I^b_{90\mu m}$
1	303.4160	-43.9837	0.56 ± 0.03	23.77 ± 0.03	22.28 ± 2.07	46.26 ± 0.00	62.64 ± 0.00
2	303.3522	-43.9848	0.36 ± 0.19	19.43 ± 0.10	22.86 ± 2.06	57.54 ± 0.83	68.47 ± 0.80
3	303.2306	-43.8065	0.42 ± 0.07		22.26 ± 2.06	38.49 ± 1.59	47.14 ± 1.62
4	303.1724	-43.8871	0.56 ± 0.05		22.43 ± 2.11	30.44 ± 0.68	43.82 ± 0.81
5	302.9638	-43.7682	0.89 ± 0.02		21.02 ± 2.03	9.62 ± 0.05	15.83 ± 0.08
6	302.7813	-42.4777	4.60 ± 0.89	23.82 ± 2.00	20.88 ± 2.37	1.41 ± 0.00	2.10 ± 0.00
7	302.6293	-46.4968	4.23 ± 0.34	33.13 ± 14.81	31.22 ± 3.42	0.12 ± 0.05	2.31 ± 0.00
8	302.1944	-44.8284	1.07 ± 0.04		21.71 ± 1.77	10.31 ± 0.13	19.03 ± 0.24
9	302.0468	-44.9842	0.56 ± 0.01		22.05 ± 2.18	43.73 ± 0.08	52.67 ± 0.26
10	302.0361	-44.9538	0.47 ± 0.09	22.21 ± 1.09	22.65 ± 2.33	47.11 ± 2.16	50.70 ± 2.06
11	301.9879	-44.9723	0.38 ± 0.16		21.72 ± 2.09	26.84 ± 0.00	30.51 ± 0.00
12	301.9201	-45.5506	0.59 ± 0.01	17.85 ± 0.01	21.64 ± 2.33	2.79 ± 0.00	7.69 ± 0.00
13	301.6525	-44.9388	0.87 ± 0.29		21.66 ± 2.34	10.80 ± 0.22	20.11 ± 0.15
14	301.6106	-45.0572	0.81 ± 0.02		22.37 ± 2.07	42.62 ± 0.00	58.40 ± 0.00
15	301.5995	-45.1168	0.19 ± 0.03		21.31 ± 2.04	16.37 ± 0.18	30.23 ± 0.49
16	301.5767	-45.1257	0.74 ± 0.03		21.27 ± 2.32	14.80 ± 0.00	25.64 ± 0.00
17	301.6581	-44.1975	1.19 ± 0.00		20.96 ± 2.03	1.26 ± 0.05	5.35 ± 0.03
18	301.5848	-44.9657	0.93 ± 0.02		20.72 ± 2.14	17.08 ± 0.09	23.78 ± 0.09
19	301.6505	-44.1871	1.20 ± 0.01		20.40 ± 1.91	1.23 ± 0.00	5.55 ± 0.00
20	301.5607	-45.0648	0.93 ± 0.02		22.48 ± 2.35	25.86 ± 1.45	36.60 ± 1.95
21	301.4967	-45.1017	1.02 ± 0.00		21.22 ± 2.57	17.96 ± 0.41	24.182 ± 0.11
22	301.4725	-45.0704	1.05 ± 0.01		21.28 ± 2.30	20.45 ± 0.00	29.81 ± 0.00
23	301.4683	-44.6991	1.03 ± 0.00	17.66 ± 0.01	21.70 ± 1.77	2.90 ± 0.09	7.93 ± 0.12
24	301.3154	-44.9915	0.69 ± 0.03		20.55 ± 2.15	10.63 ± 0.32	17.27 ± 0.38

Notes:
[a]gl and gb are the Galactic longitude and latitude in degrees (°).
[b]The MIR and FIR data are in units of MJy sr^{-1}.

Table 4.4: Rank correlations (ρ) with corresponding p-values among the IR and FUV data for our observed locations.

Wavelength	1004 Å		1058 Å		1117 Å		1157 Å	
	ρ	p-value	ρ	p-value	ρ	p-value	ρ	p-value
8 μm	-0.1117	0.630	-0.2649	0.246	-0.2702	0.236	-0.2922	0.199
24 μm	0.2000	0.704	-0.0286	0.957	-0.0286	0.9572	-0.0285	0.957
22 μm	-0.3273	0.147	-0.2792	0.220	-0.3273	0.147	-0.3000	0.186
65 μm	0.0285	0.902	0.1714	0.457	0.1501	0.516	0.1753	0.447
90 μm	0.0740	0.749	0.2130	0.354	0.1903	0.408	0.2129	0.354

Wavelength	1250 Å		1500 Å		1750 Å	
	ρ	p-value	ρ	p-value	ρ	p-value
8 μm	-0.3857	0.084	-0.4064	0.067	-0.4103	0.064
24 μm	-0.0857	0.872	-0.0857	0.872	0.1428	0.787
22 μm	0.1883	0.414	0.1351	0.559	0.1481	0.522
65 μm	0.4844	0.026	0.4338	0.049	0.4675	0.033
90 μm	0.4558	0.038	0.4025	0.070	0.4312	0.051

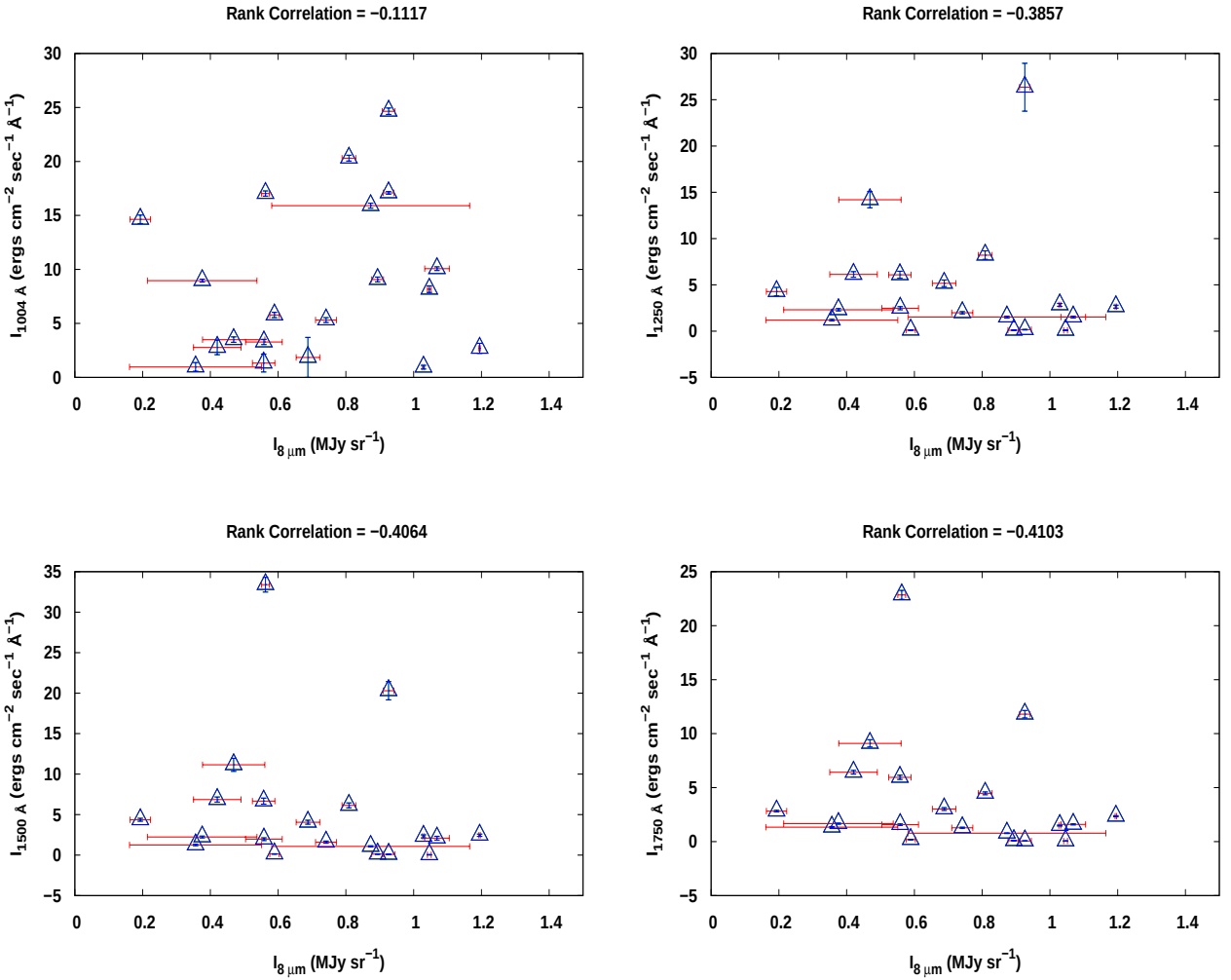

Figure 4.2: Correlation plots for 8 μm vs. 1004, 1250, 1500 and 1750 Å intensities.

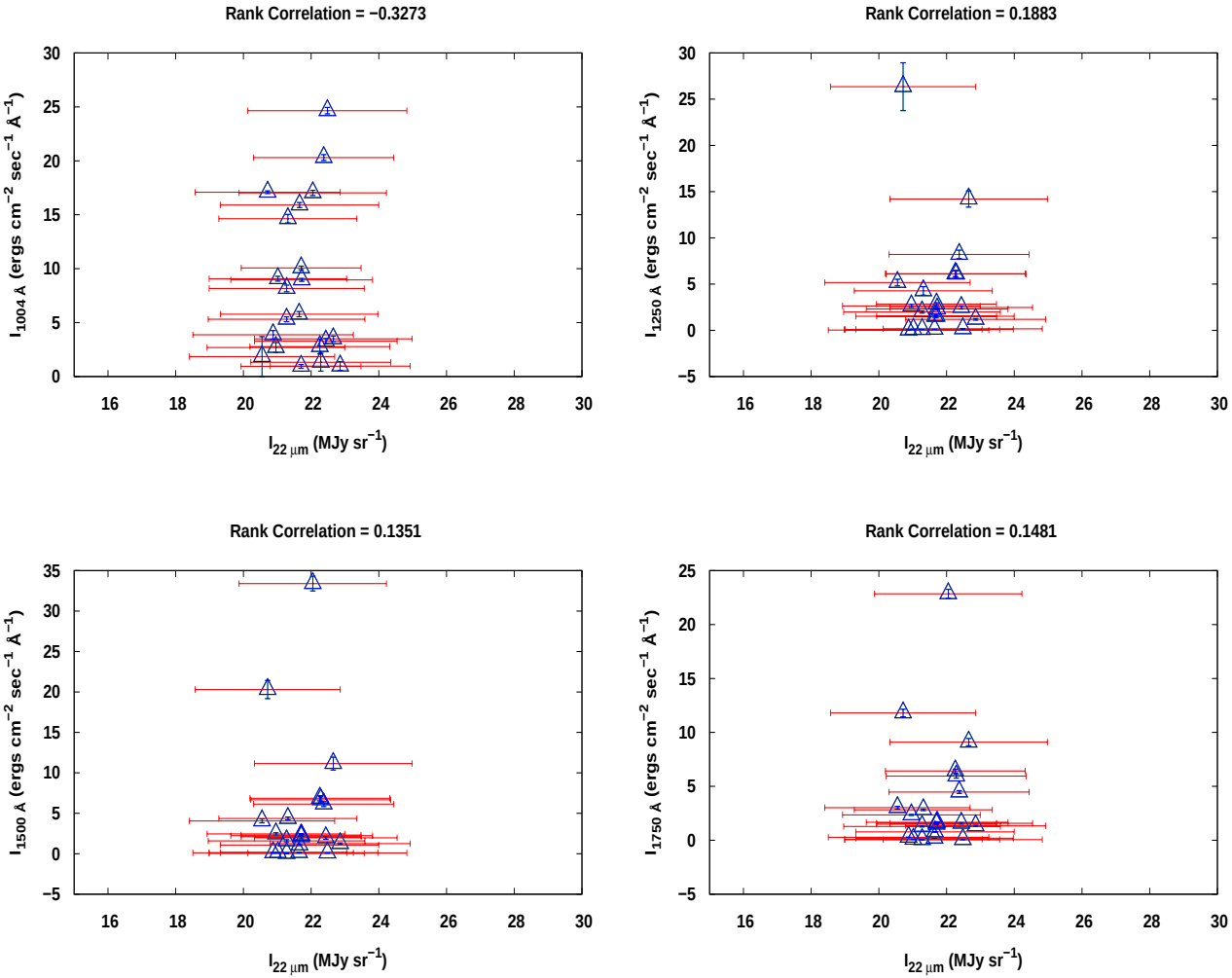

Figure 4.3: Correlation plots for 22 μm vs. 1004, 1250, 1500 and 1750 Å intensities.

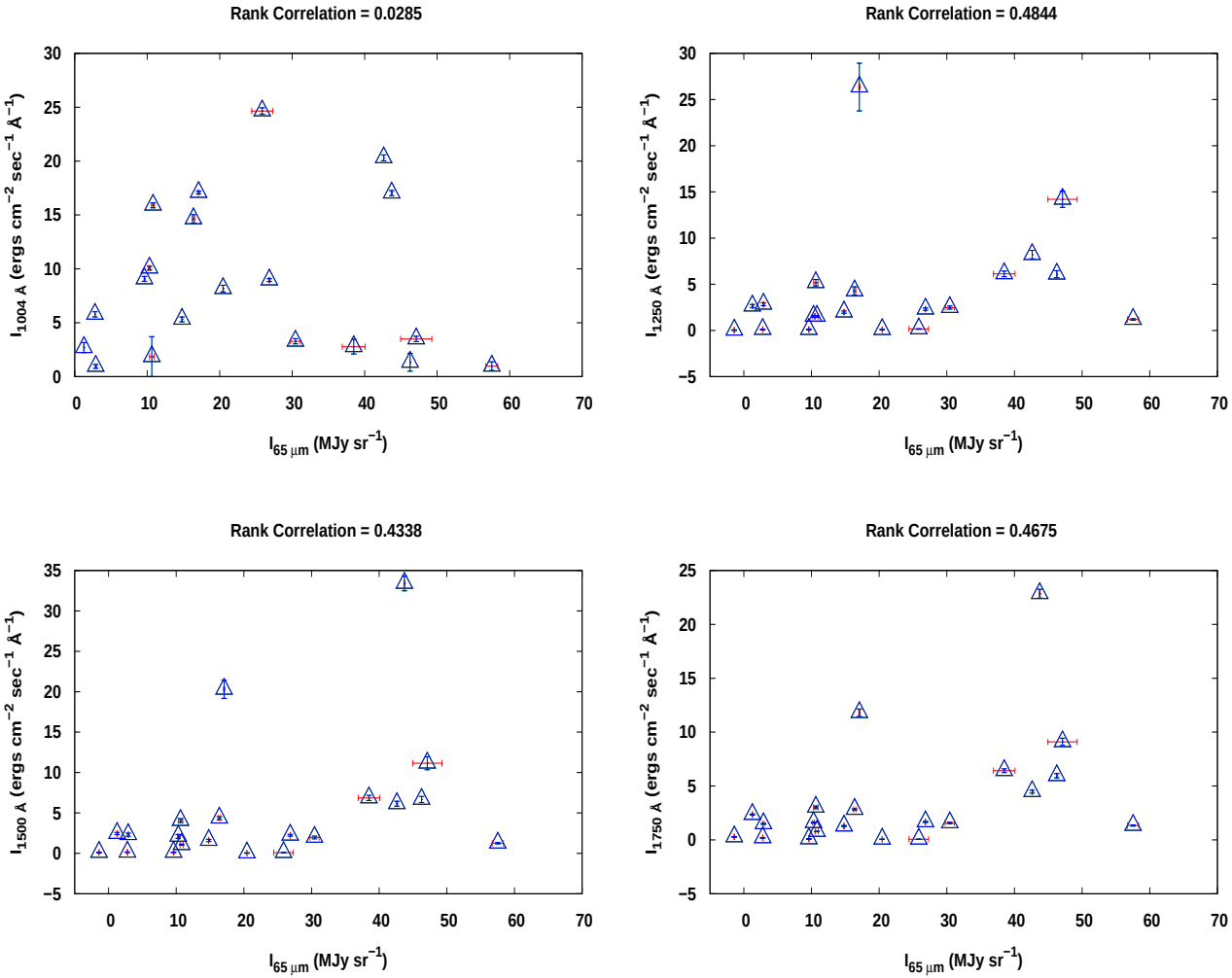

Figure 4.4: Correlation plots for 65 μm vs. 1004, 1250, 1500 and 1750 Å intensities.

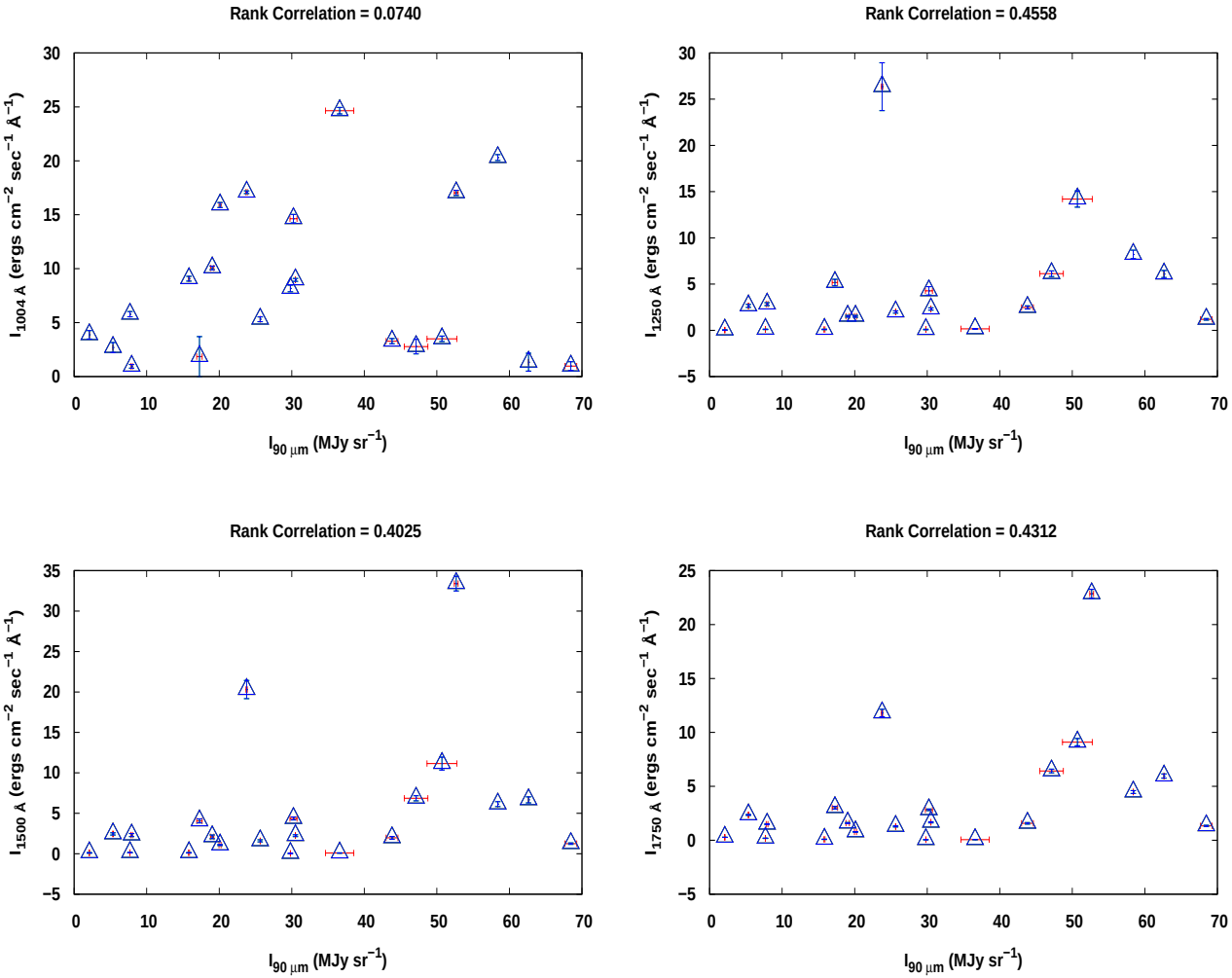

Figure 4.5: Correlation plots for 90 μm vs. 1004, 1250, 1500 and 1750 Å intensities.

Table 4.5: Rank correlations (ρ) with corresponding p-values among the MIR and FIR data for our observed locations.

Wavelength	ρ	p-value
8 vs. 24 μm	0.0857	0.872
8 vs. 22 μm	-0.4922	0.023
8 vs. 65 μm	-0.6675	0.001
8 vs. 90 μm	-0.6649	0.001
24 vs. 65 μm	-0.1428	0.787
24 vs. 90 μm	-0.0857	0.872
22 vs. 24 μm	-0.1428	0.787
22 vs. 65 μm	0.7662	5.120e-05
22 vs. 90 μm	0.7896	2.077e-05
65 vs. 90 μm	0.9818	3.570e-15

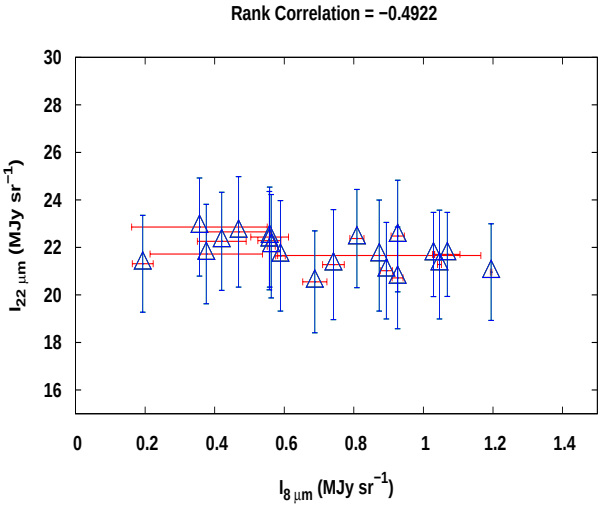

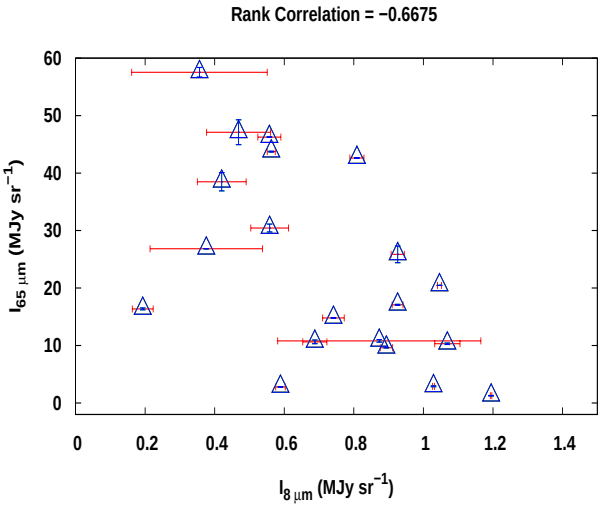

Figure 4.6: Correlation plots for MIR (8, 22 μm) and FIR (65 μm) intensities.

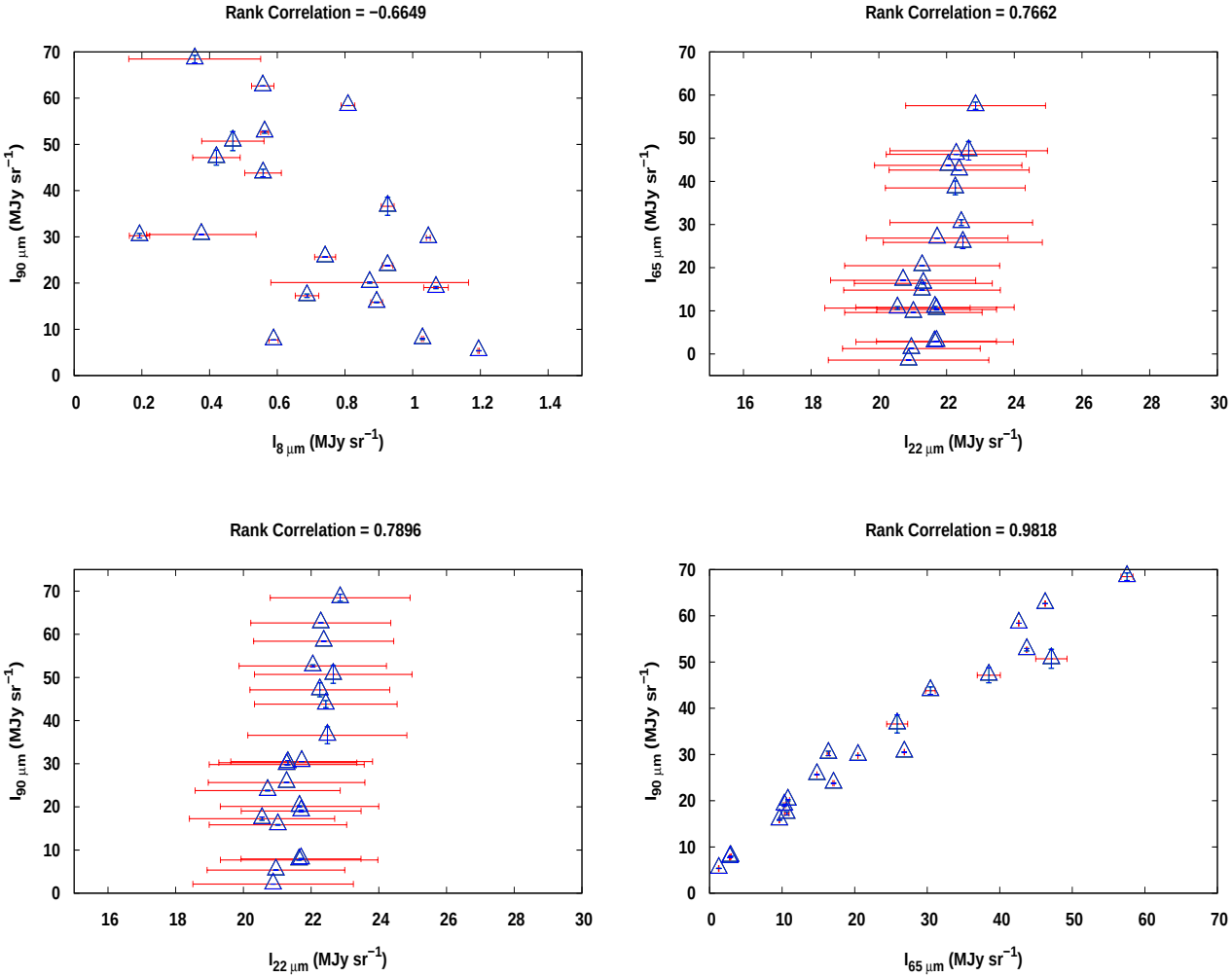

Figure 4.7: Correlation plots for MIR (8, 22 μm) and FIR (65, 90 μm) intensities.

4.4 Discussion and Conclusions

We see from Table 4.4 that the correlation coefficients for the MIR vs. FUV data are very close to zero with high p-values which indicate the acceptance of null hypothesis, i.e. no correlation or association. Therefore, we can say that no reliable correlation is observed between the MIR and the FUV emissions. Now, we already know that 8 μm corresponds to emission from PAH molecules and 24 μm corresponds to hot dust emission where the dust grain type depends on the surroundings. For our observed locations, the nearest documented source of emission to each diffuse location lies between 3–25′ (using SIMBAD database), with the closest source for 18 of the 24 locations being RGB/AGB stars. Among the rest of the locations in Tables 4.1, 4.2 and 4.3, two are close to supernovae remnants, one is close to an X-ray source, two are close to O/B stars and one location is close to an HII region.

Sandstrom et al. (2010, 2011) [153, 165] state that the PAH abundance is relatively high in molecular regions but generally very low under the typical diffuse ISM conditions. The faint 8 μm emission in the SMC is attributed to the destruction of PAHs which were ejected to the diffuse ISM after formation in the atmospheres of diffuse stars. The PAH fraction is also suppressed in HII regions. Since our diffuse locations do not coincide with either of the locations observed by Gordon et al. (2003) [21] or Apellaniz & Rubio (2012) [141] (Figure 4.1), we can interpret the absence of a correlation between the 8 μm and FUV emissions (Figure 4.2) as a lack of PAHs at our 24 observed locations which can be attributed to the presence of high radiation emitting sources that are favourable for their destruction in the diffuse ISM. Now, Oey et al. (2017) [166] state that the VSGs that produce 24 μm emission are more resilient to UV radiation. Hence, our observed lack of 22 μm vs. FUV correlations (Figure 4.3) seem to indicate that the emissions observed by us do not come from VSGs but from hot large dust grains. This is supported by the good correlations values observed between 22 μm and the FIR (65 and 90 μm) intensities in Table 4.5. The correlation values indicate a similar nature and origin of the dust grains showing emission at 22, 65 and 90 μm which is also evident from the very good correlation between 65 and 90 μm intensities (Table 4.5, Figures 4.6 and 4.7).

The better correlations for FIR vs. FUV with lower p-values (<0.05) (Table 4.4, Figures 4.4 and 4.5) as compared to MIR vs. FUV indicate that the 65 and 90 μm emission is seen from larger dust particulates near regions emitting high radiation (e.g. supernovae remnants, hot stars) which cause the destruction

of smaller VSGs and PAH molecules. The FIR vs. 1250 Å correlation is relatively better among them which implies that the dust scattering is more at 1250 Å as compared to the other FUV wavelengths. The negative correlation observed between 8 μm and the FIR (65 and 90 μm) intensities in Table 4.5 (Figures 4.6 and 4.7) show that the emissions from one source decreases as the other increases which is due to the destruction of smaller PAHs while larger grains remain intact. This is also seen from the negative 8 μm vs. 22 μm correlations which shows that the emissions come from different types of dust populations. Seok et al. (2014) [167] mention that PAH deficiency might also occur due to coagulation on to larger dust grains. Although they mention that this process is dominant in metal-rich galaxies, the negative correlations observed here might also indicate such PAH coagulation onto larger grains showing FIR emissions which may lead to the weaker PAH emissions in the SMC.

The SMC is a low-metallicity galaxy as compared to the LMC or MW which causes lower line blanketing in stellar atmospheres leading to the destruction of PAHs by harder UV fields [153]. PAHs might be destroyed in low-metallicity galaxies by hard UV radiation from massive stars [168] or by supernova shocks [167, 169]. In Chapter 3, we have studied the rank correlations between IR (*Spitzer*: 8 and 24 μm) and FUV (*FUSE*: 1004-1159 Å) data for 43 locations in the LMC and found a very good correlation ($\sim$0.8) for both 8 μm vs. FUV and 24 μm vs. FUV intensities. These results were obtained for locations near HII regions which shows how PAHs and small dust grains are shielded from destruction in high-metallicity galaxies even in the presence of star-forming regions. The effects of the UV field from massive star formation regions or supernova shocks can be spread over a much larger area in low-metallicity galaxies with a decreased dust-to-gas ratio [153, 170]. The LMC-like shielding effect seems to be absent in the low-metallicity SMC which might have led to the absence of 8 μm vs. FUV correlation.

In conclusion, we have studied the IR-FUV correlations for 24 diffuse locations in the SMC and we found the FIR (65 μm, 90 μm) dust emissions to be better correlated to the FUV intensities as compared to the MIR (8 μm, 22 μm, 24 μm) emissions. The absence of 8 μm vs. FUV correlation, coupled with the weakness of emission seen near 8 μm, indicates a lack or absence of PAHs at our observed diffuse locations due to their possible destruction by high energetic radiation fields in the vicinity. The FIR vs. FUV correlations (Figures 4.4 and 4.5) indicate a strong contribution towards heating of the larger dust grains showing emission at our locations by UV photons predom-

inantly scattered around 1250 Å. The very good correlation between the 65 μm and 90 μm intensities (Figure 4.7) indicates that the grains responsible for both these emissions belong to similar dust environments. A comparison between the absence of MIR vs. FUV correlations for the SMC and the very good correlations obtained for the LMC (in Chapter 3) seems to support the theory that PAHs are shielded from destruction in high-metallicity galaxies as opposed to the low-metallicity SMC.